Supplementary Information

Spatially Engineered Polymer-in-Salt Electrolytes for Solid-State Lithium–Sulfur Batteries

Haeli Lee,[a] *Nagyeong Shin,*[a] *Taehyun Kim,*[a] *Minho Jung,*[a] *Seung Gi Jung,*[a] *Jinhan Cho,* [a] *Holger Althues,*[b] *and Jun Hyuk Moon**[a]

[a]Department of Chemical and Biological Engineering, Korea University, 145 Anam-ro, Seongbuk-gu, Seoul, 02841, Republic of Korea

[b]Fraunhofer Institute for Material and Beam Technology IWS, Winterbergstrasse 28, Dresden, 01277, Germany

* Corresponding author: junhyukmoon@korea.ac.kr

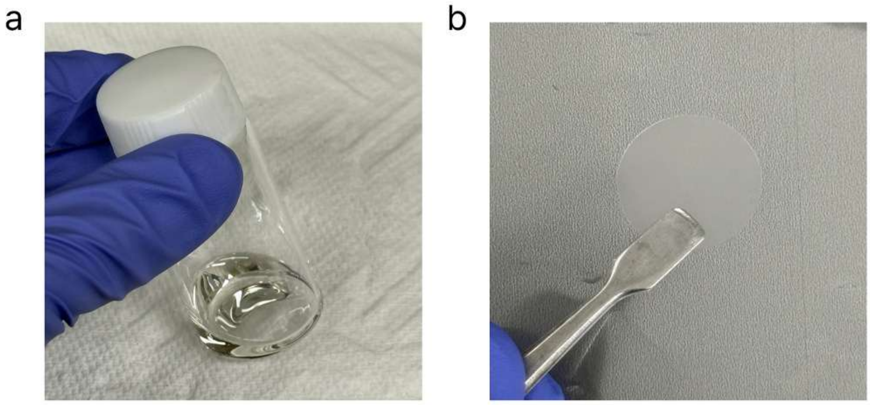

Fig. S1. Digital image of the (a) PIS electrolyte solution (b) solid-state PIS film obtained by casting. The film is prepared using a doctor blade with a controlled thickness of 20 μm.

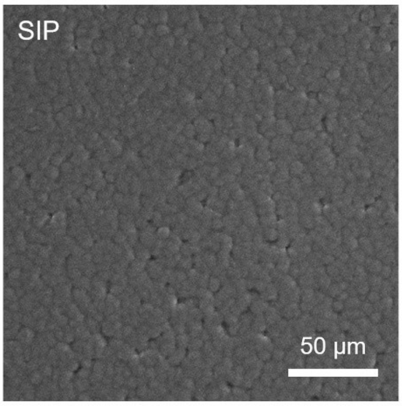

Fig. S2. SEM image of the SIP electrolyte film. Compared with PIS, the lower salt content results in reduced porosity after drying.

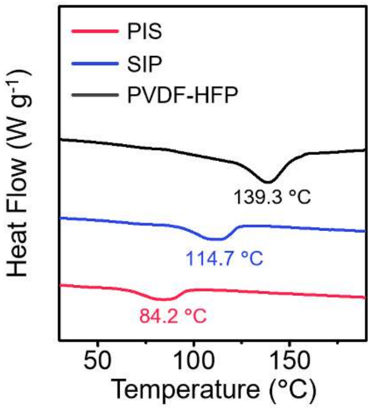

Fig. S3. DSC curves of PIS, SIP, and pristine PVDF-HFP, showing their respective glass transition temperatures.

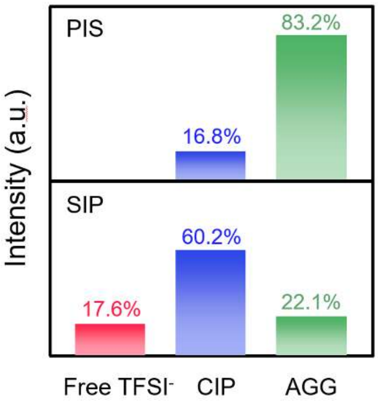

Fig. S4. Comparison of the relative fractions of free TFSI⁻, CIP, and AGG in PIS and SIP, obtained from Raman spectra.

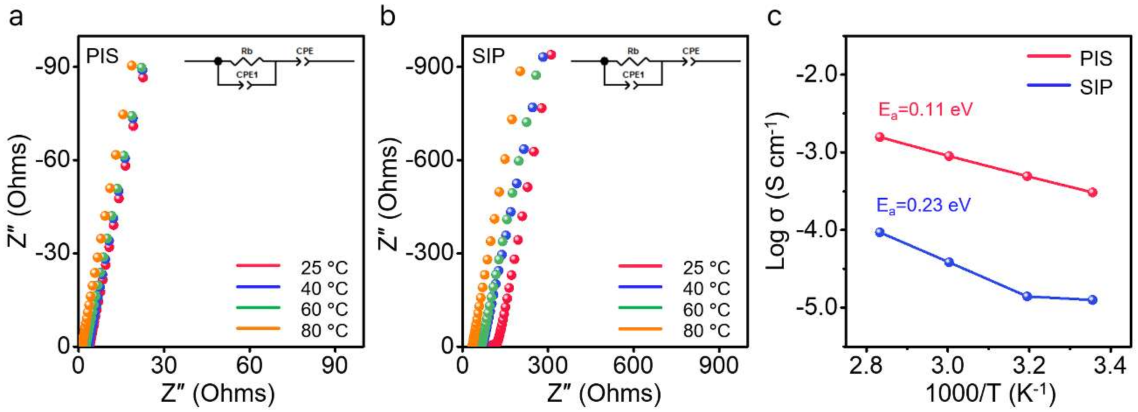

Fig. S5. (a) EIS of PIS and (b) SIP at different temperatures, with insets showing the equivalent circuits. (c) Arrhenius plots of ionic conductivity for PIS and SIP, with activation energies indicated.

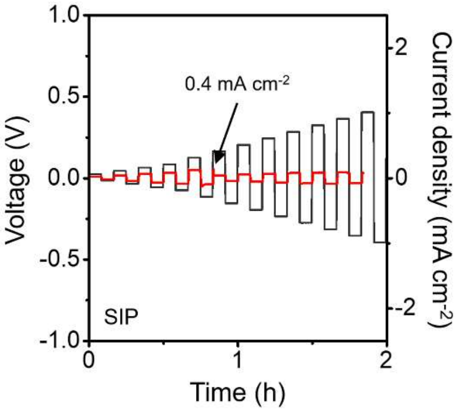

Fig. S6. CCD of SIP measured in Li symmetric cells, showing a sharp voltage drop and short circuit at ~0.4 mA cm^{-2}.

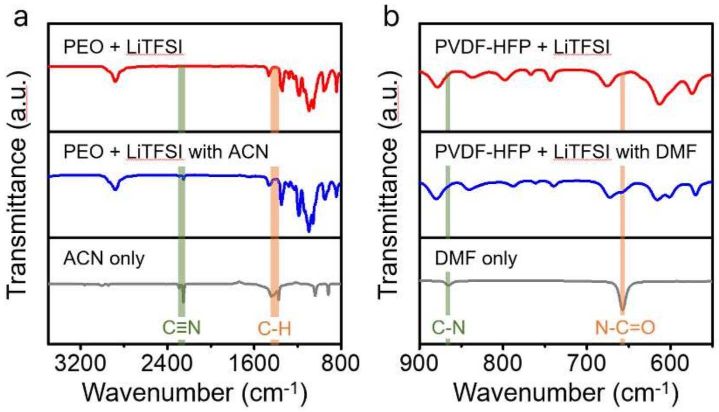

Fig. S7. FT-IR spectra of (a) PEO+LiTFSI and (b) PVDF-HFP+LiTFSI before drying (with ACN or DMF) and after drying, shown together with the spectra of pure ACN and DMF. Characteristic peaks associated with free ACN (2293 and 2254 cm^{-1}) and free DMF (658 or 866 cm^{-1}) are detectable in the polymer samples before drying but do not appear in the dried films used for cell assembly, where only the characteristic signals of PEO (2870 cm^{-1}) and PVDF-HFP (876 cm^{-1}) are observed.

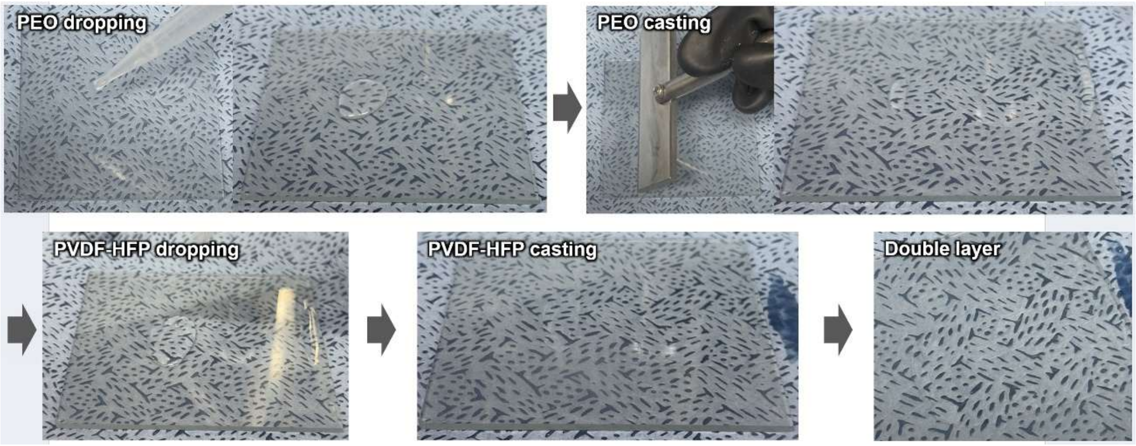

Fig. S8. Digital images of the sequential PEO/PVDF-HFP double-layer casting process.

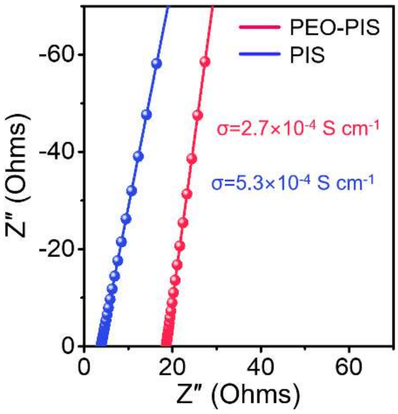

Fig. S9. EIS of PEO-PIS and PIS, with ionic conductivities obtained from the plots.

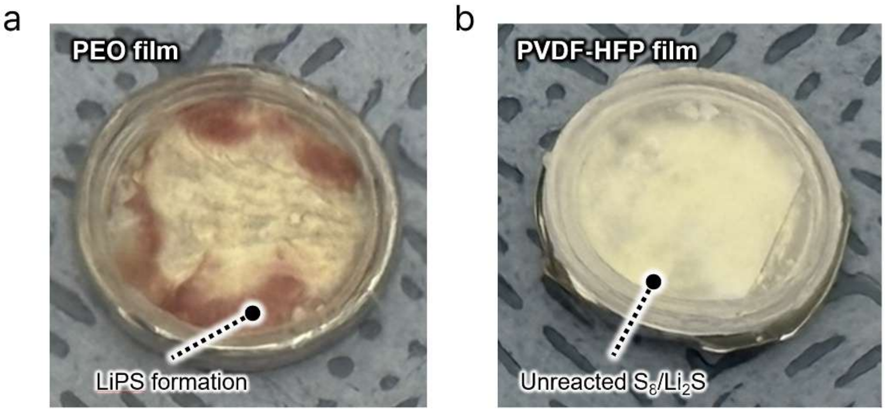

Fig. S10. Optical images of (a) PEO and (b) PVDF-HFP films after contact with S/Li_2S mixtures at 30 °C.

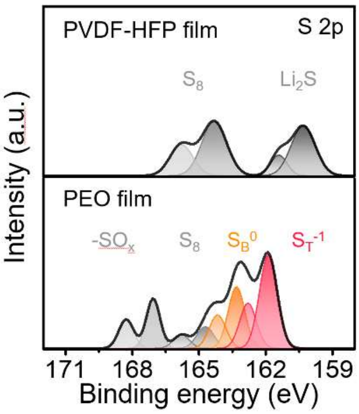

Fig. S11. S 2p XPS spectra of PVDF-HFP and PEO films after contact with S/Li_2S mixtures at 30 °C.

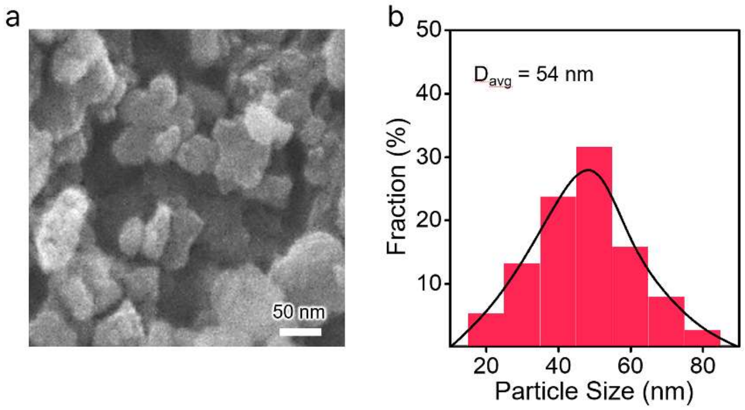

Fig. S12. (a) SEM image and (b) particle size distribution of ball-milled LATP nanofillers.

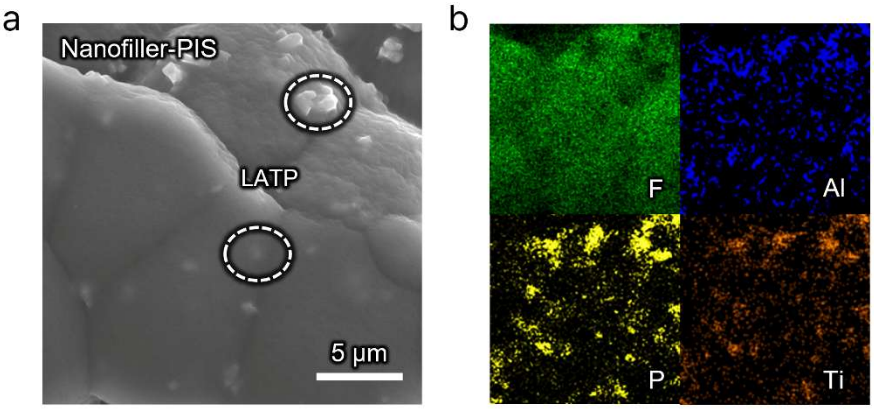

Fig. S13. (a) SEM and (b) elemental mapping images of Nanofiller-PIS.

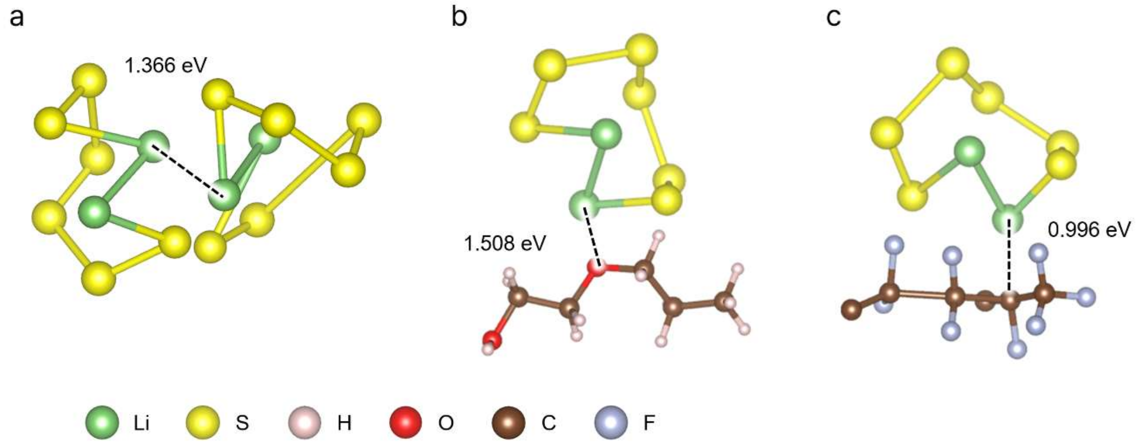

Fig. S14. (a) Li_2S_6–Li_2S_6 cohesive interaction (1.366 eV), (b) Li_2S_6–PEO solvation interaction (1.508 eV), and (c) Li_2S_6–PVDF-HFP solvation interaction (0.996 eV). The solvation potential (ΔΔG), defined as the difference between solvation energy and cohesive energy, is 0.142 eV for PEO and −0.370 eV for PVDF-HFP, indicating favorable LiPS solvation in PEO.

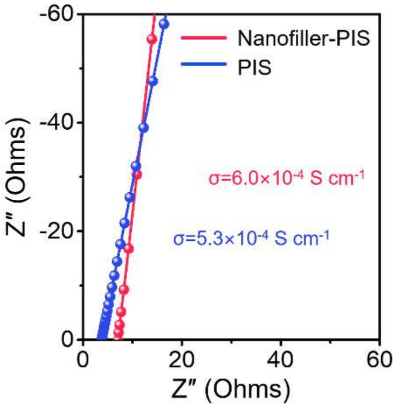

Fig. S15. EIS of Nanofiller-PIS and PIS, with ionic conductivities extracted from the plots.

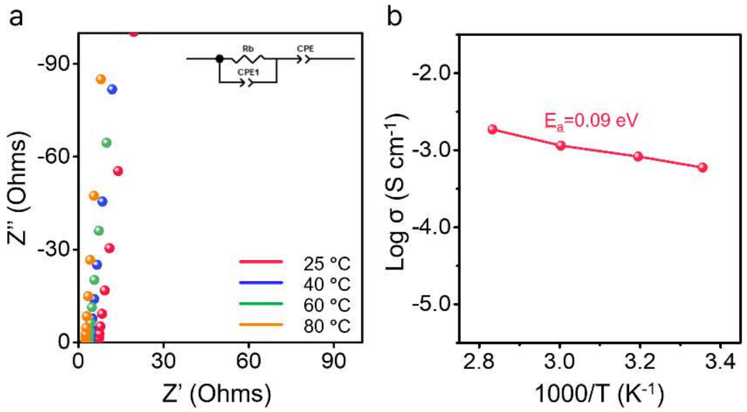

Fig. S16. (a) EIS of Nanofiller-PIS at different temperatures, with the equivalent circuit shown in the inset. (b) Arrhenius plot of ionic conductivity, with activation energy indicated.

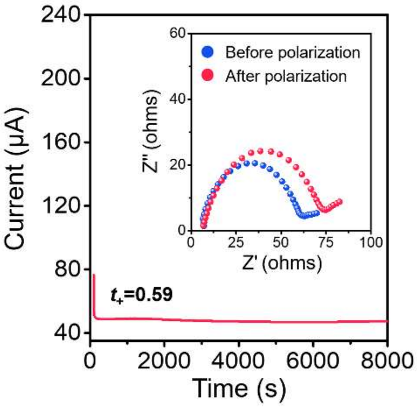

Fig. S17. Time–current profile for Li^+ transference number measurement of Nanofiller-PIS. The initial current (I_0=76.42 μA) and steady-state current (I_{ss}=47.51 μA) are used to calculate t_+=0.59. The inset shows EIS spectra before and after polarization.

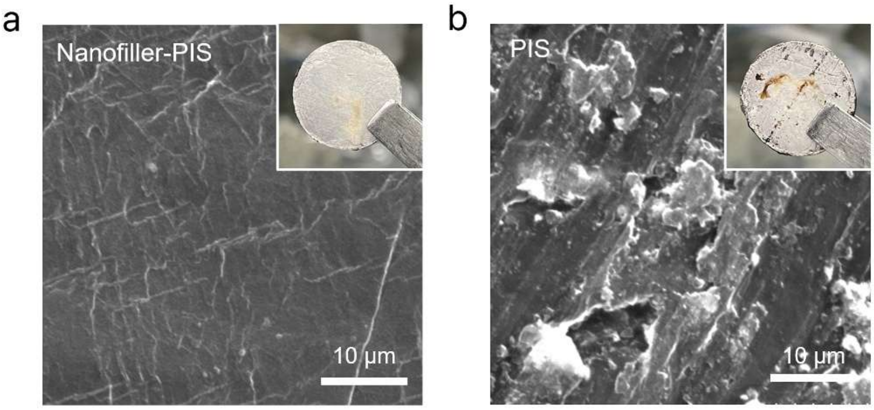

Fig. S18. SEM images of the Li surface in symmetric cells with (a) Nanofiller-PIS and (b) PIS electrolytes after cycling for 300 h at 0.5 mA cm^{-2} and 0.5 mAh cm^{-2}.

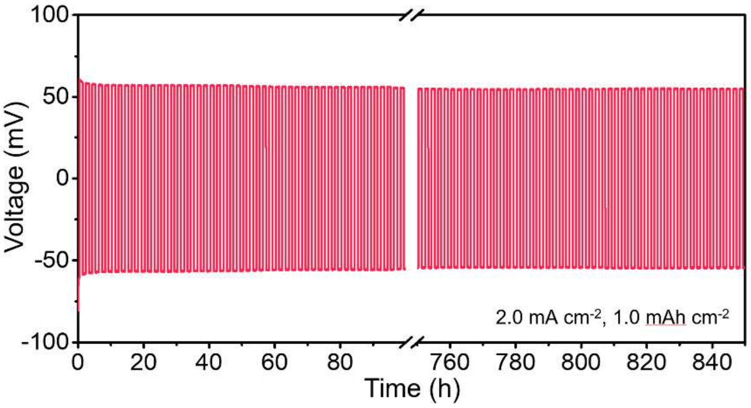

Fig. S19. Li stripping/plating profile of Nanofiller-PIS in symmetric cells at 2.0 mA cm^{-2} with a capacity of 1.0 mAh cm^{-2}. Stable cycling is maintained for over 800 h with an overpotential of ~57 mV.

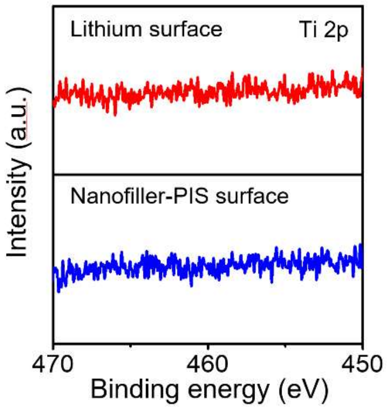

Fig. S20. Ti 2p XPS spectra of the lithium surface (top) and the Nanofiller-PIS surface (bottom).

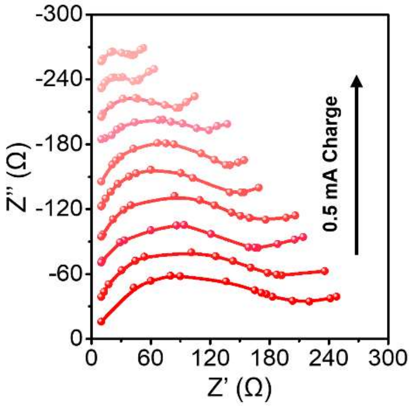

Fig. S21. Operando EIS of Nanofiller-PIS Li symmetric cells measured at 0.5 mA cm^{-2} in 30 min intervals. The interfacial resistance gradually decreases with continued cycling.

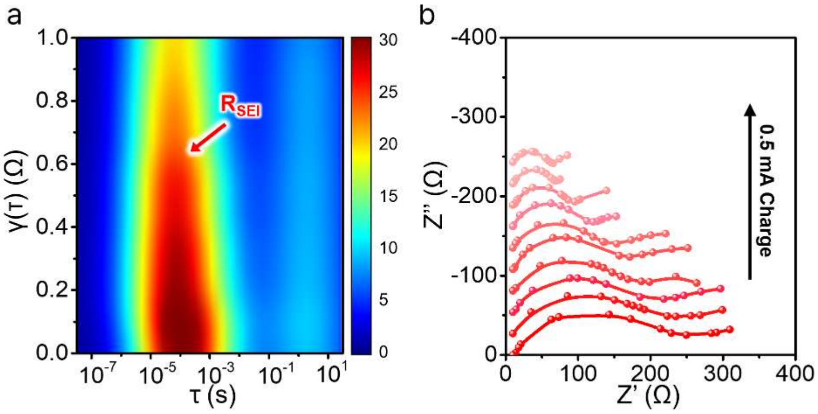

Fig. S22. Operando EIS and DRT analysis of PIS Li symmetric cells measured at 0.5 mA cm^{-2} in 30 min intervals.

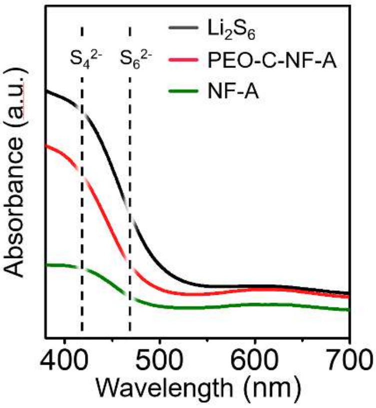

Fig. S23. Ex-situ UV–Vis spectra collected at 2.1 V during discharge. In the PEO-C-NF-A cell, clear absorption features corresponding to LiPS species were detected at ~420 nm (S_4^{2-}) and ~470 nm (S_6^{2-}). In contrast, these signals were weak in the NF-A cell, indicating significantly reduced LiPS presence without the PEO layer.

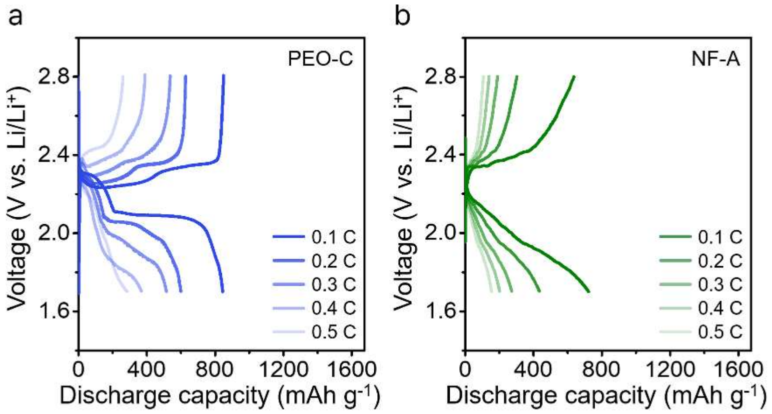

Fig. S24. Charge/discharge profiles of (a) PEO-C, and (b) NF-A cells at various C-rates (0.1–0.5 C). The PEO-C cell delivers 845 mAh g^{-1} at 0.1 C and 290 mAh g^{-1} at 0.5 C. The NF-A cell delivers 722 mAh g^{-1} at 0.1 C and 155 mAh g^{-1} at 0.5 C.

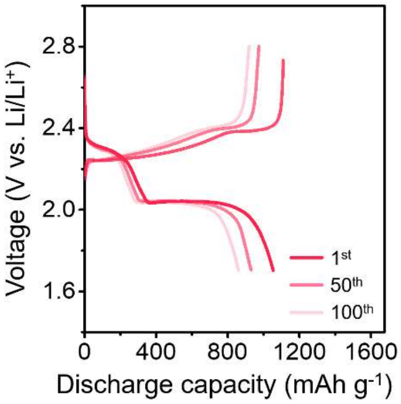

Fig. S25. Charge/discharge profiles at different cycles for a cell with a sulfur loading of 1 mg cm^{-2} at 0.2 C. The initial capacity is 1050 mAh g^{-1}, which decreases to 933 mAh g^{-1} after 50 cycles and 863 mAh g^{-1} after 100 cycles.

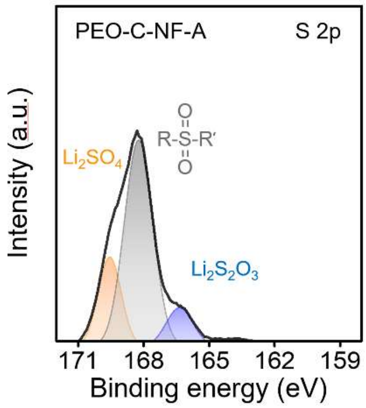

Fig. S26. S 2p XPS spectrum of the Li metal anode after 5 cycles in the PEO-C-NF-A cell. The S 2p spectra show only Li_2SO_4, Li_2SO_3, and R–SO_x–R′ species associated with the LiTFSI-derived SEI. No Li_2S or Li_2S_2 peaks (161.3 and 162.5 eV) were detected, indicating that shuttle-driven side reactions did not occur.

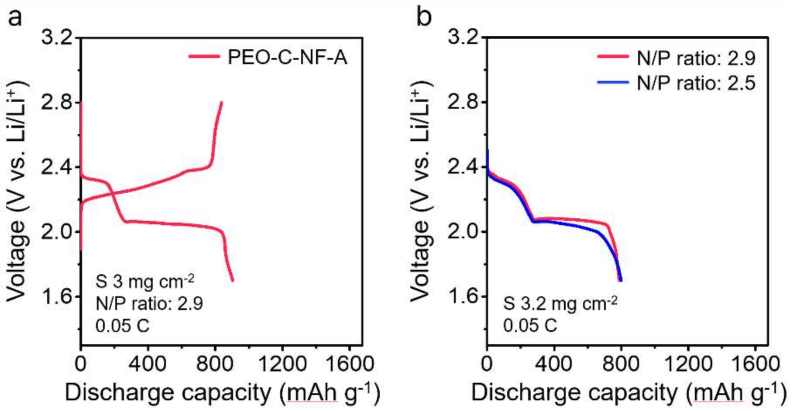

Fig. S27. Galvanostatic discharge profiles of the PEO-C-NF-A cell with sulfur loading of 3 mg cm^{-2} and N/P ratio of 2.9 (left) and 3.2 mg cm^{-2} and N/P ratio of 2.5, 2.9 (right) at 0.05 C.

Table. S1. Cell performance comparison with previously reported literature employing all-solid-state electrolytes

Electrolyte	Specific capacity (mAh g^{-1})	Sulfur loading (mg cm^{-2})	C-rate	Cycle	Decay per cycle	Retention (%)	Temperature (°C)	ref
This work	**1050**	**1**	**0.2**	**120**	**0.199**	**78**	**30**	**-**
PEO-PAN	1200	-	0.1	75	0.539	66.7	70	[1]
PEGDA-LLAZO	1055	1	0.2	50	0.178	91.5	50	[2]
Poly-DOL	800	0.7	0.1	100	0.287	75	30	[3]
PVDF	840	1-2	0.03	60	3.5	75	55	[4]
PEO	833	0.5	0.2	50	0.68	95.9	60	[5]
LPSCl	850	1.2	0.2	50	0.387	82	40	[6]

References

[1] J. Sheng, Q. Zhang, C. Sun, J. Wang, X. Zhong, B. Chen, C. Li, R. Gao, Z. Han and G. Zhou. Crosslinked nanofiber-reinforced solid-state electrolytes with polysulfide fixation effect towards high safety flexible lithium–sulfur batteries, Advanced Functional Materials, 32, 40 (2022), 2203272.

[2] C. Yan, Y. Zhou, H. Cheng, R. Orenstein, P. Zhu, O. Yildiz, P. Bradford, J. Jur, N. Wu and M. Dirican. Interconnected cathode-electrolyte double-layer enabling continuous Li-ion conduction throughout solid-state Li-S battery, Energy Storage Materials, 44, (2022), 136–144.

[3] X. Meng, Y. Liu, Y. Ma, Y. Boyjoo, J. Liu, J. Qiu and Z. Wang. Diagnosing and Correcting the Failure of the Solid-State Polymer Electrolyte for Enhancing Solid-State Lithium–Sulfur Batteries, Advanced Materials, 35, 22 (2023), 2212039.

[4] R. Fang, H. Xu, B. Xu, X. Li, Y. Li and J. B. Goodenough. Reaction mechanism optimization of solid-state Li–S batteries with a PEO-based electrolyte, Advanced Functional Materials, 31, 2 (2021), 2001812.

[5] Y. Liu, H. Liu, Y. Lin, Y. Zhao, H. Yuan, Y. Su, J. Zhang, S. Ren, H. Fan and Y. Zhang. Mechanistic investigation of polymer-based all-solid-state lithium/sulfur battery, Advanced Functional Materials, 31, 41 (2021), 2104863.

[6] J. Zhou, M. L. Holekevi Chandrappa, S. Tan, S. Wang, C. Wu, H. Nguyen, C. Wang, H. Liu, S. Yu and Q. R. Miller. Healable and conductive sulfur iodide for solid-state Li–S batteries, Nature, 627, 8003 (2024), 301–305.